Nano Energy 58 (2019) 202–210

Contents lists available at ScienceDirect

Nano Energy

journal homepage: www.elsevier.com/locate/nanoen

Full paper

Phase transition in two-dimensional tellurene under mechanical strain modulation

Yuan Xiang[a], Shengjie Gao[b], Rong-Guang Xu[a], Wenzhuo Wu[b,*], Yongsheng Leng[a,*]

[a] Department of Mechanical and Aerospace Engineering, The George Washington University, Washington, DC 20052, USA
[b] School of Industrial Engineering, Purdue University, West Lafayette, IN 47907, USA

ARTICLE INFO

Keywords:
Tellurene
Phase transition
Density functional theory (DFT)
2-D materials
Strain engineering
Elastic modulus

ABSTRACT

We carry out computational simulations based on density functional theory (DFT) to investigate different phases of two-dimensional (2-D) tellurene. These phases are classified by their characteristic space groups and symmetry elements. Correlations of these phases to the bulk crystalline tellurium structure are also illustrated. Our specific interests include mechanical property calculations for different phases and the possible phase transitions between them. Simulation results show that these 2-D Te phases have very different elastic moduli due to their different atomic bonding and relaxed structures. Moreover, compression along the in-plane directions facilitates the α → β phase transition, while in-plane tensile strains always make the α-phase more stable than the β-phase. However, the energy difference between the two phases is comparable to or even much smaller than the thermal energy *kT*, depending on the in-plane strain direction. We find that further increase of the tensile strain along the chain direction beyond a critical value, ca. 12%, may lead to a possible α → γ phase transition. As the tensile strain is above 15%, the γ-phase will be more stable than the α-phase, accompanied by a further reduced transition energy barrier.

1. Introduction

Two-dimensional (2-D) tellurene (atomically thin Te) has recently attracted much attention in both theoretical and experimental studies due to its intriguing properties [1–19]. For example, it has a process-modulated bandgap in the range of 0.35–1.2 eV [20], which is superior to graphene. Tellurene also has higher carrier mobility (~10^4 cm^2/Vs) at room-temperature than transition metal dichalcogenides (TMDs). Moreover, tellurene is air-stable, which is advantageous than phosphorene [1,17,21]. All of these appealing characteristics suggest the potential of 2-D Te as a new material platform for constructing high-performance functional nanodevices.

Substantial theoretical and experimental studies on the 2-D Te have been carried out. Experimental studies have been focusing on the synthesizing of 2-D Te with low-cost, facile and rapid routes. A breakthrough has been achieved in solution-synthesizing this 2-D material with large lateral sizes (~100 μm), process-controlled thickness (from a monolayer to tens of nm) and high yield (> 90%) [1]. Other methods based on molecular-beam epitaxy have also been reported [2,22]. Theoretical studies, on the other hand, concentrate on finding new phases of 2-D Te and revealing their different properties based on quantum mechanical density functional theory (DFT) calculations [4–7, 9, 10, 20]. It has been found that 2-D Te has more than five stable or meta-stable phases. Among them, at least two phases have been observed in experiments [1,2,22]. All of these phases have very different mechanical and electrical properties, which are of great importance to the designing and manufacturing nanodevices in the future semiconductor industry [10,15,20]. Although theoretical studies have made progress in discovering new phases, there are significant inconsistencies in defining 2-D Te phases from different research groups (such as using different names to describe the same phases [7, 10, 15, 20]). Here, we report a systematic study on the tellurene phases based on the space group of material symmetry.

Phase transition of 2-D Te is another fundamental issue that has been less addressed. It is well known that the properties of materials can be modulated through phase transition [23–25]. For example, strain modulation can switch the thermodynamic stability among three stable monolayer TMDs [26–37], leading to the tuning of band gaps and photoluminescence. However, the phase transition of 2-D Te under mechanical strain modulation has not yet been fully investigated.

In this paper, we focus on the study of three fundamental issues: (1) classifying different 2-D Te phases based on their space group and their relationship with the bulk Te; (2) calculating elastic modulus of different 2-D Te phases; and (3) studying possible phase transitions of 2-D

* Corresponding authors.
E-mail addresses: wenzhuowu@purdue.edu (W. Wu), leng@gwu.edu (Y. Leng).

https://doi.org/10.1016/j.nanoen.2019.01.040
Received 16 December 2018; Received in revised form 12 January 2019; Accepted 13 January 2019
Available online 15 January 2019

Te under different strain loadings. Our specific interest is to investigate how the mechanical strain changes the energy of each phase and to calculate the transition energy barriers between them. In particular, our findings may explain why different experimental groups obtained different 2-D Te phases [1,2,22], revealing the role of the substrate chosen may have a significant impact on the 2-D Te phases. This work is expected to shed light on the application of tellurene as 2-D phase transition materials for applications in electronics, optoelectronics, and piezotronics [38].

2. Computational simulation method

The Vienna ab initio Simulation Package (VASP) [39] with the projector-augmented wave method [40,41] is used for all of the DFT simulations. The Perdew–Burke–Ernzerhof (PBE) [42] form within the generalized gradient approximation (GGA) [43] is employed for the exchange-correlation functionals. The plane-wave cutoff energy is set to 500 eV. A vacuum space of around 20 Å normal to the tellurene slab surface is introduced to avoid interactions between the computational cell and its images. The Tkatchenko and Scheffler (DFT-TS) method [44] is used for the treatment of van der Waals correction, which shows better agreement with the experimental data of the optimized lattice parameters of the bulk Te [15]. Calculations with different van der Waals methods, including the DFT-D2 [45] and D3 [46] methods of Grimme are also performed. We find a negligible effect on the elastic modulus of tellurene reported in this paper. We use the Γ-centered Monkhorst-pack [47] k-point sampling for the Brillouin zone integration and find that the $15 \times 11 \times 1$ grid is sufficient for the convergence. In some calculations which require higher-accuracy energy values, a $21 \times 15 \times 1$ grid is employed. All atoms in the computational cell are relaxed until the forces are less than 0.01 eV $Å^{-1}$. Convergence criterion for electronic relaxations is set to be 10^{-6} eV. The climbing image nudged elastic band (CI-NEB) method [48] is used to determine the energy barrier during the phase transition.

3. Simulation results

3.1. 2-D Te Phases

In the bulk phase, each Te atom is covalently bonded with its two nearest neighbors on the same Te chain. Individual Te helical chains are stacked together by non-covalent bonding (Fig. 1). However, this non-covalent interaction exhibits somewhat covalent-like feature. Therefore, sometimes it is called "covalent-like quasi-bonding" (CLQB) [15,20,49,50]. Bulk tellurium belongs to the space group $P3_121$ (see the unit cell within the parallelogram in Fig. 1**a**), which contains a three-fold screw axis along the [0001] direction (Fig. 1**b**). This space group belongs to the D_3 group in Schoenflies notation [51,52]. Note that all of the Te atoms in the unit cell are equivalent in Fig. 1. Different colored atoms shown in the figure are to derive different 2-D phases from the bulk, which will be discussed below. Depending on the cleavage method and surface relaxation, there are at least four known phases, namely, α-, β-, γ-, and δ-phases [15], as shown in Figs. 2–5. We follow the nomenclature given previously [15] to define different 2-D Te phases, in which the alphabetical order represents the formation energy of these phases within a few layers (specifically, up to seven layers [15], see Fig. S1) in ascending order. In this paper, we define the "directions" and the "layer" in each 2-D Te phase as:

3.1.1. Directions

We assume that the thickness direction of all the 2-D Te phases is always along the *z*-direction and the chain direction ([0001] direction in bulk) for the α-, β- and δ-phases is defined as the *y*-direction. For the γ-phase, because of the loss of its original chain structures in the bulk phase due to atomic reconstructions (Fig. 4**d**), we define the *y*-direction along the armchair direction, and the *x*-direction is along the zig-zag direction (see Fig. 4**c**).

3.1.2. Layer

For the definition of the "layer" in each 2-D Te phase [4–7,9,10,20], we use the lower case "*layer*" to represent all the atoms with the same *z*-coordinate and the capital "*Layer*" to represent all covalently-bonded neighbors. Thus the notations "*1 l*" and "*1 L*" as illustrated in Figs. 2–5 represent the thickness of a specific layer of atoms.

3.1.3. The α-phase

Cutting along the parallel $\{10\bar{1}0\}$ planes of the bulk Te (red dotted lines in Fig. 1**a**) results in a stable 2-D α-phase Te. The thickness of the slab depends on the distance between the two cutting planes. For example, we show an α-phase slab with two *Layers* in Fig. 2**a–c** and a slab with five *Layers* in Fig. 2**d**. Due to the surface relaxation and changes in the bond lengths, helical chains lose the threefold screw axis along the *y*-direction (Fig. 2**a**). The twofold (screw) axis along the *x*-direction (magenta line in Fig. 2**a**) is formed, resulting in the space group $P2_1$ α-phase for even *Layers* (Fig. 2**a**) and the space group P2 α-phase for odd *Layers* (Fig. 2**d**). Both the $P2_1$ and P2 groups belong to the group C_2 in Schoenflies notation. The significant change in the space group of the corresponding tellurium 2-D slabs when being thinned down from the bulk implies that these 2-D materials will have very different physical properties, such as the electrical conductivity, the elasticity, the piezoelectric effect, and the nonlinear optical properties [51,52]. For instance, the elastic compliance component, s_{15}, should be zero for the bulk Te, but will have a non-zero value for the 2-D α-phase Te. Fig. 2**d** also shows that significant bond length relaxations occur at outmost *Layers*. This atomic structural relaxation gradually decays towards the interior *Layers*. Thus, it is clear that the interior region of a *thick* 2-D α-phase Te will have the same property as the bulk Te, while it is only in the *surface* region that a different property should be observed.

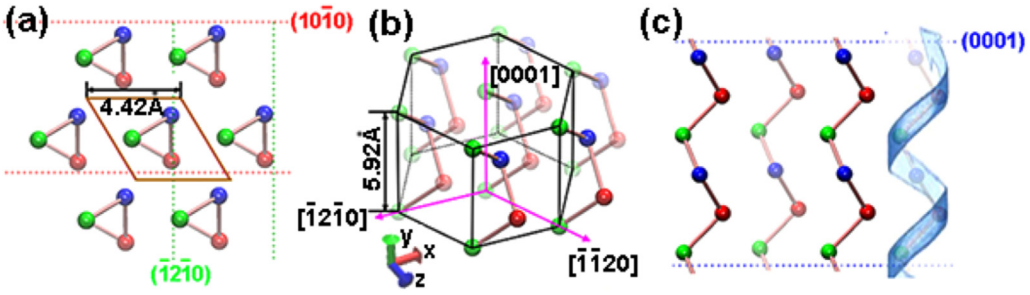

Fig. 1. Atomic configurations of the bulk Te from different views: (a) (0001) plane, (b) the perspective view, and (c) $(\bar{1}2\bar{1}0)$ plane. The brown parallelogram in (a) shows the primitive cell of the bulk phase. The red and green dotted lines in (a) and the blue dotted line in (c) show the $\{10\bar{1}0\}$, $\{\bar{1}2\bar{1}0\}$, and {0001} parallel planes, respectively. The helical chiral chain structure in (c) is also illustrated using blue belt. Note that all of the Te atoms in the unit cell are equivalent. Different colored atoms shown here are for the purpose of deriving different 2-D phases from the bulk.

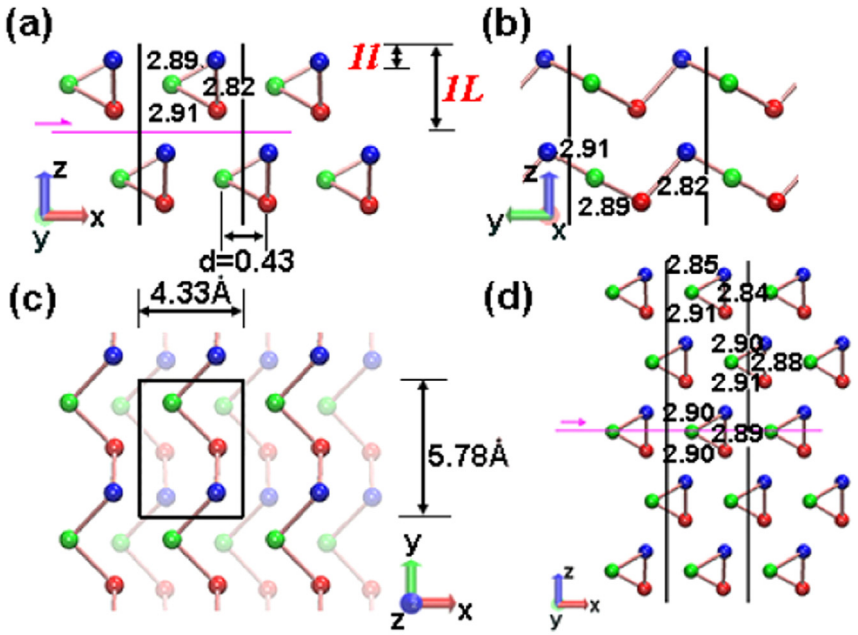

Fig. 2. The two-*Layer* α-phase: (a) *xz*-plane (front), (b) *yz*-plane (side), and (c) *xy*-plane (top) views. The *x*- and *y*-directions are along the $[\bar{1}2\bar{1}0]$ and [0001] of the original bulk phase, respectively. The magenta *half* arrow in (a) shows the twofold *screw* axis ($P2_1$) along the *x*-direction. The length of each relaxed bond is also illustrated in Å. The definitions of 1 *layer* (1 *l*) and 1 *Layer* (1 *L*) are marked in red fonts in (a). The definition of the fractional distance *d* is also shown in (a). The DFT unit cell is shown in (c) with the vacuum indicated in (a). (d) The atomic configuration of a five-*Layer* α-phase. The magenta *full* arrow shows the twofold rotation axis (P2) along the *x*-direction. Note that the atomic structure relaxation gradually decays from the outmost *Layer* to the interior *Layers*.

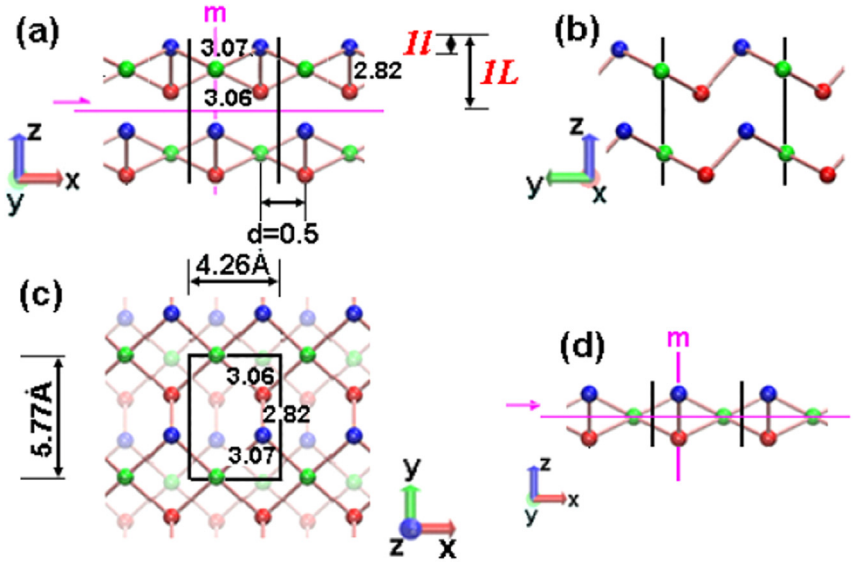

Fig. 3. The two-*Layer* β-phase: (a) *xz*-plane (front), (b) *yz*-plane (side), and (c) *xy*-plane (top) views. The *x*- and *y*-directions are along the $[\bar{1}2\bar{1}0]$ and [0001] of the original bulk phase, respectively. The magenta *half* arrow in (a) shows the twofold screw axis along the *x*-direction and the magenta vertical line in (a) indicates a mirror plane (*m*). The length of each relaxed bond is also illustrated in Å. The definitions of 1 *layer* (1 *l*) and 1 *Layer* (1 *L*) are marked in red fonts in (a). The definition of fractional distance *d* is also shown in (a). The DFT unit cell is shown in (c). (d) The atomic configuration of a single-*Layer* β-phase. The magenta *full* arrow shows the twofold rotation axis (P2) along the *x*-direction.

3.1.4. *The β-phase*

This phase can be thought of as derived from the α-phase by slightly shifting the mid-*layer* Te atoms (the green atoms in Fig. 3**a**) towards their closest neighboring helical chains, resulting in the periodic mirror (m) planes perpendicular to the *x*-direction (Fig. 3**a**). The corresponding space groups are $P2_1/m$ for even *Layers* (Fig. 3**a**) and P2/m for odd *Layers* β-phase (Fig. 3**d**), which are both classified as the Schoenflies C_{2h} space group. We define a fractional distance (*d*) as the ratio of the projected distance between the neighboring helical chains along the *x*-direction to the lattice constant in the *x*-direction (Figs. 2**a** and 3**a**). Note that fractional distance *d* can be used as a geometrical indicator to distinguish α-phase from β-phase. The slab is classified as a β-phase with $d = 0.5$, and any *d* values lower than 0.5 should correspond to an α-phase (see Section 3.3 discussion). According to our calculation, the 1 *L* α-phase is not stable and spontaneously transforms into the 1 *L* β-phase (Fig. 3**d**). However, for multiple-*Layer* tellurene, the energy of the α-phase is always lower than that of the β-phase.

3.1.5. *The γ-phase*

Cutting the bulk helical chains into integer 3*l*, 6*l*, 9*l*, …, 3n*l* *layers* by

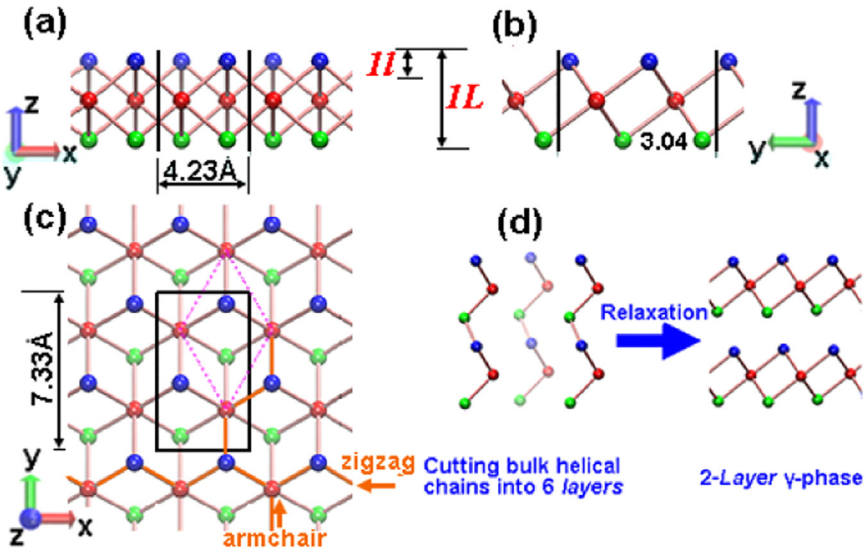

Fig. 4. The single-*Layer* γ-phase: (a) *xz*-plane (front), (b) *yz*-plane (side), and (c) *xy*-plane (top) views. The orange arrows in (c) show the zigzag-direction (*x*-direction) and the armchair-direction (*y*-direction). All bonds have the same length of 3.04 Å, as illustrated in (b). The definitions of 1 *layer* (1 *l*) and 1 *Layer* (1 *L*) are marked in red fonts in (a). The DFT unit cell is shown in (c). Note that the vacuum in this phase is along the [0001] direction of the original bulk phase. (d) The formation of γ-phase. The vacuum is above and below the slab geometry (in the [0001] direction of the original helical chains).

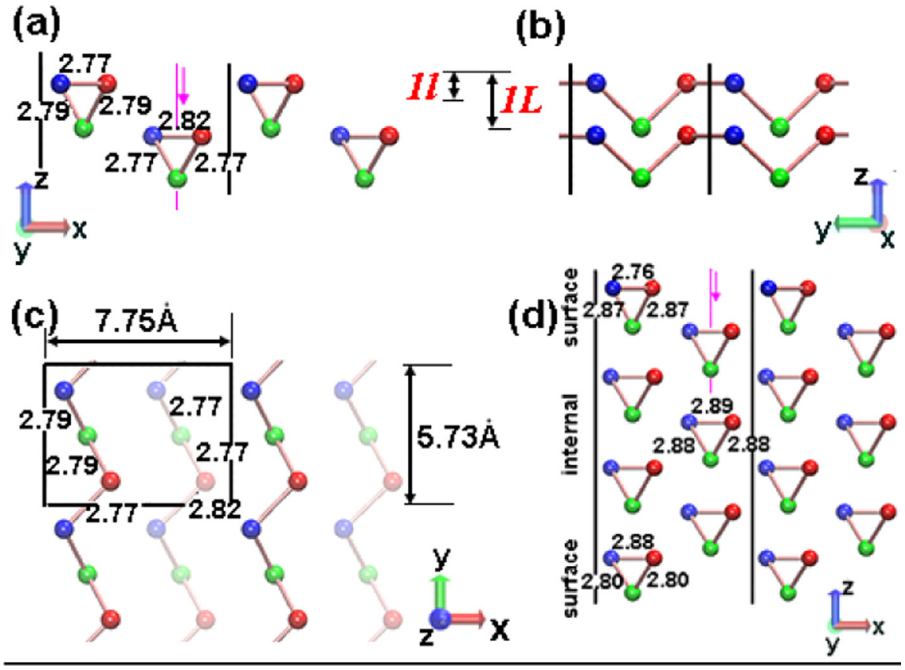

Fig. 5. The two-*Layer* δ-phase: (a) *xz*-plane (front), (b) *yz*-plane (side), and (c) *xy*-plane (top) views. The *x*- and *y*-directions are along the $[10\bar{1}0]$ and [0001] of the original bulk phase. The magenta arrow in (a) shows the twofold rotation axis along the *z*-direction. The length for each bond is also illustrated in Å. The definitions of 1 *layer* (1 *l*) and 1 *Layer* (1 *L*) are marked in red fonts in (b). The DFT unit cell is shown in (c). The vacuum in this phase is along the $[\bar{1}2\bar{1}0]$ direction of the original bulk phase. (d) The atomic configuration of a δ-phase with seven *Layers*. The surface and interior regions undergo different degrees of atomic relaxations. Note that the interior *Layers* are closed-packed.

{0001} planes (blue dotted lines in Fig. 1**c**) and allowing full relaxation of the slab geometry will result in the γ-phase Te [15](Fig. 4**d**). Different from the α- and β- phases, the thickness direction of the γ-phase is along the original ([0001]) chain direction of the bulk. Because of the high surface energy of the freshly cut dangling bonds along this direction, the relaxation of this structure is dramatic. The final equilibrium γ-phase Te is significantly different from the previous two phases, completely losing the original chain structure in the bulk phase. This γ-phase Te has a very similar structure to the 1T-MoS_2, which belongs to the $P\bar{3}m1$ space group (D_{3d} in Schoenflies notation) that has the threefold rotation axis along the *z*-direction. The primitive cell of the γ-phase is shown within the magenta parallelogram in Fig. 4**c**. For the convenience of elastic modulus and energy barrier calculations, we adopt an orthorhombic unit cell, as shown within the black rectangle in Fig. 4**c**.

3.1.6. *The δ-phase*

Cutting along the two parallel $\{\bar{1}2\bar{1}0\}$ planes (green dotted lines in Fig. 1**a**) results in a δ-phase Te (Fig. 5). Similar to the α-phase, this δ-phase Te also maintains the helical chains. However, these helical chains are not close-packed on the surface, resulting in very high surface energy thus the highest formation energy among all phases with a thickness up to five *Layers* [15](see Fig. S1). This high surface energy also makes the 1 *L* δ-phase unstable according to our calculations. As the number of *Layers* is gradually increased, this high-energy surface is compensated by the closed-packed interior Layers (see Fig. 5**d** for the 7 *L* δ-phase), giving rise to formation energy comparable to those of the α- and β-phases, which is even lower than that of the γ-phase (see Fig.

Table 1
Summary of the 2-D Te phases based on symmetry elements.

Phase	Space group	Schoenflies notation	Major feature
α	$P2_1$ (even *Layers*) P2 (odd *Layers*)	C_2	Twofold axis along the *x*-direction. Helical chains maintained
β	$P2_1/m$ (even *Layers*) $P2/m$ (odd *Layers*)	C_{2h}	Twofold axis along the *x*-direction with mirror planes perpendicular to this axis
γ	$P\bar{3}m1$	D_{3d}	Threefold axis along the *z*-direction
δ	*P*2	C_2	Twofold axis along the *z*-direction. Helical chains maintained.

S1) [15]. Note that the twofold rotation axis of the δ-phase is perpendicular, rather than parallel, to the slab surface (Fig. 5**a and d**), which is different from all other phases. The space group of the δ-phase is P2 (C_2 in Schoenflies notation) for both the odd and even *Layers*. Table 1 summarizes the basic features of different 2-D Te phases.

3.2. Elastic modulus

We calculate the elastic modulus of each 2-D Te phase by applying a biaxial strain ε. The elastic modulus C is calculated according to [53–55]:

$$C = \frac{1}{A_0}\frac{\partial^2 E}{\partial \varepsilon^2}\Big|_{\varepsilon=0} \quad (1)$$

where A_0 is the equilibrium in-plane area of the simulation cell, and E is the energy at specific strain ε. The energy E is calculated based on a 3×3 unit-cell grid with ε ranging from -0.004–0.004 with a strain increment of 0.001. All of the atoms in the simulation cell are fully relaxed under strain. We calculate the elastic modulus C for up to four *Layers* for each phase and confirm a linear relationship of the elastic modulus C versus the 2-D Te thickness. These computational results are shown in Fig. 6. Values for the single-*Layer* α- and δ-phases are not available because they are not stable in the single-*Layer* phases. From the figure, it is seen that the γ- and β-phases have higher elastic moduli, largely because of the covalent bonding character in their in-plane directions (Figs. 4**c and** 3**c**). For the α- and δ-phases, both intra-chain covalent and inter-chain non-covalent interactions exist in the two in-plane directions, making them more compliant compared to the γ- and β-phases.

As far as we know, experimental data for elastic moduli for different 2-D Te phases are still not available. Here we compare our calculations with other elemental and Te-based 2-D materials, as well as some 2-D chalcogenides, as illustrated in Fig. 6. These include single-*Layer* elastic

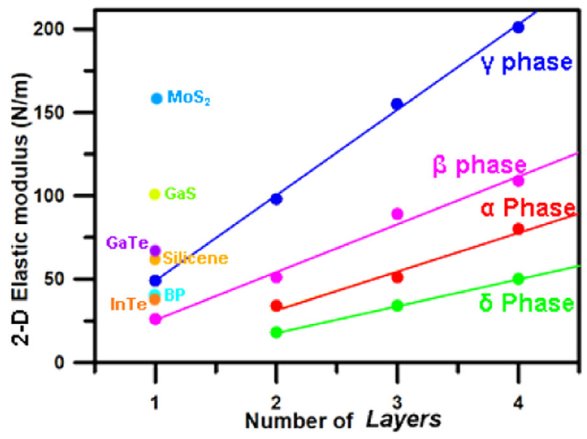

Fig. 6. Elastic moduli of 2-D Te phases up to four *Layers*. The elastic moduli of other single *Layer* elemental and Te-based 2-D materials, as well as 2-D chalcogenides, are also shown in the figure for comparison. The elastic moduli of silicene, GaTe, InTe, BP, MoS_2 and GaS in this figure are all from the DFT calculations (from reference 54–56).

modulus of silicene (62 N/m, DFT) [56], GaTe (66 N/m, DFT), InTe (39 N/m, DFT) [55], black phosphorus (BP) (22 N/m in the armchair direction and 56 N/m in the zigzag direction, DFT and experiment) [57,58], MoS_2 (165 N/m, DFT; 180 N/m, experiment), and GaS (98 N/m, DFT) [55]. While the elastic moduli of different single-*Layer* tellurene phases are comparable with those of elemental and Te-based 2-D materials, they are significantly lower than the elastic modulus of 2-D sulfides. This indicates that 2-D Te materials are more compliant to be likely modulated by mechanical strains.

We attribute the different elastic moduli for the four 2-D Te phases to two effects. The first is related to the bonding type between atoms in each phase. For α- and δ-phases, they both have covalent intra-chain bonding in the chain direction and CLQB inter-chain interactions. However, for β-and γ-phases, covalent bonding exists in the two in-plane directions (see Figs. 2**c,** 3**c,** 4**c and** 5**c**). As the strength of the CLQB is weaker than covalent bonding, the elastic moduli of the α- and δ-phases will have lower values than those of the β- and γ-phases. Since the surface packing density in the δ-phase is even lower than that of the α-phase (see Figs. 2**d and** 5**d**), the δ-phase has even weaker CLQB interactions and thus has the lowest elastic modulus (Fig. 6). Moreover, strong anisotropic mechanical properties are expected for the four phases, especially for the α- and δ-phases. The second effect is related to different atomic structures in the four phases. The α-, β- and δ-phases maintain the helical chain structures (Figs. 2**a,** 3**a** and 5**a**) that are likely to be stretchable under mechanical strains, keeping the length of their covalent bonds almost unchanged. In contrast, the γ-phase completely loses the chain structure (Fig. 4). Any in-plane mechanical strains applied will lead to direct changes in its covalent bond lengths, resulting in a much higher energy cost and thus giving the highest in-plane elastic modulus.

3.3. Phase transition under mechanical strain modulation

For the above discussed four phases of 2-D Te, we are interested in two fundamental questions: (1) what are the relationships between these phases and if one phase can be transformed to another under some specific conditions? (2) how does a mechanical strain influence the phase transition? In this section, we discuss and demonstrate two possible phase transitions by calculating the energy barriers between the two phases and tuning the energy barriers with applied strains. Our calculations are based on the climbing image nudged elastic band (CI-NEB) method [48] to determine the energy barriers.

3.3.1. The α→ β phase transition

We take the 2*L* structure as a working example and employ an independent control of the lattice parameter in the *x*- or *y*-direction to calculate energy barrier variations induced by strains. We find that the slab thickness has a negligible effect on the energy barriers per atom, as well as on the threshold strain for the phase transition. Therefore, only the 2*L* slab calculations are reported in this work. In all calculations, the unit cell in the directions perpendicular to the strain direction is fully relaxed.

The energy versus reaction coordinate curves along the *x*- and *y*-directions are shown in Fig. 7**a** and **b**. A total of eight intervals are set between the 2*L* α- and 2*L* β-phases. The corresponding reaction

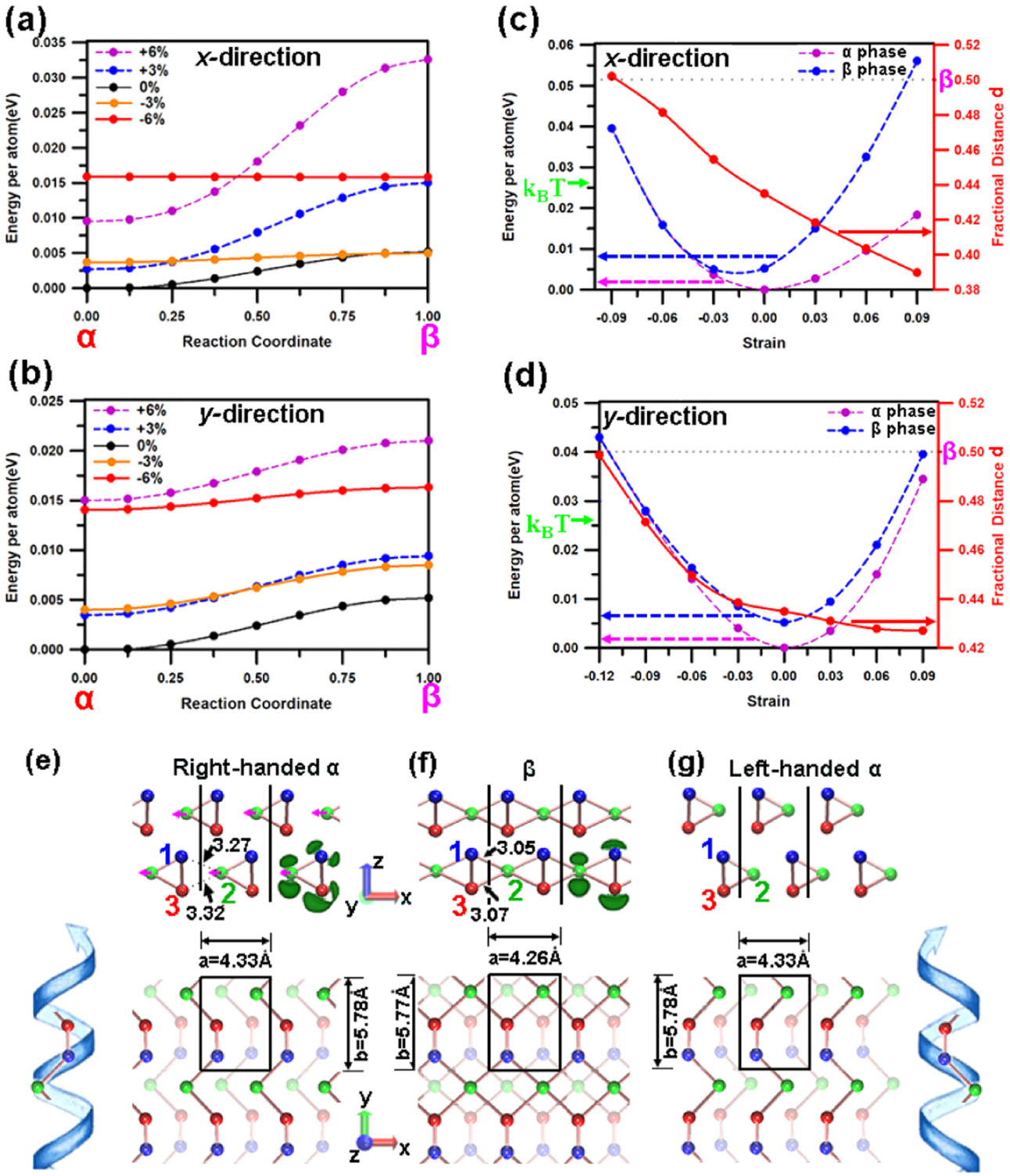

Fig. 7. The α→β phase transition: (a) and (b) show the different energy-reaction coordinate profiles versus strain along the *x*- and *y*-directions, respectively; (c) and (d) show the variations of the corresponding energy of the two phases versus strain. The fractional distance *d* versus strain is also shown in (c) and (d). Label "β" indicates the β-phase with the fractional distance *d* of 0.5. The α→ β phase transition occurs when the value of *d* reaches 0.5. (e) - (g) show the atomic configurations of the two-*Layer* right-handed α-, non-chiral β-, and left-handed α-phases, respectively. Electron localization functions (ELFs) are also shown with dark green isosurface of 0.9e $Bohr^{-3}$ in (e) and (f). Chirality is illustrated using blue belts. Atomic bond lengths are also illustrated in the unit of Å in (e) and (f). The magenta arrows in (e) show the α → β transition through moving the mid-*layer* atoms along the *x*-direction.

coordinate changes from "0" (α-phase) to "1" (β-phase) during this phase transition. The energy value of the α-phase under zero strain is taken as the reference zero. The strain-free energy difference between the two phases is around 5.189 meV/atom, corresponding to 31.2 meV for the 2 *L* unit cell, which is consistent with the previous study [15].

The equilibrium configurations of the α- and β-phase Te under zero strain are shown in Fig. 7**e** and **f**, respectively. It is seen that both α- and β-phases have almost the same lattice constants while additional covalent bonds exist in the β-phase. The α → β transition is mainly through moving the mid-*layer* green Te atoms along the *x*-direction

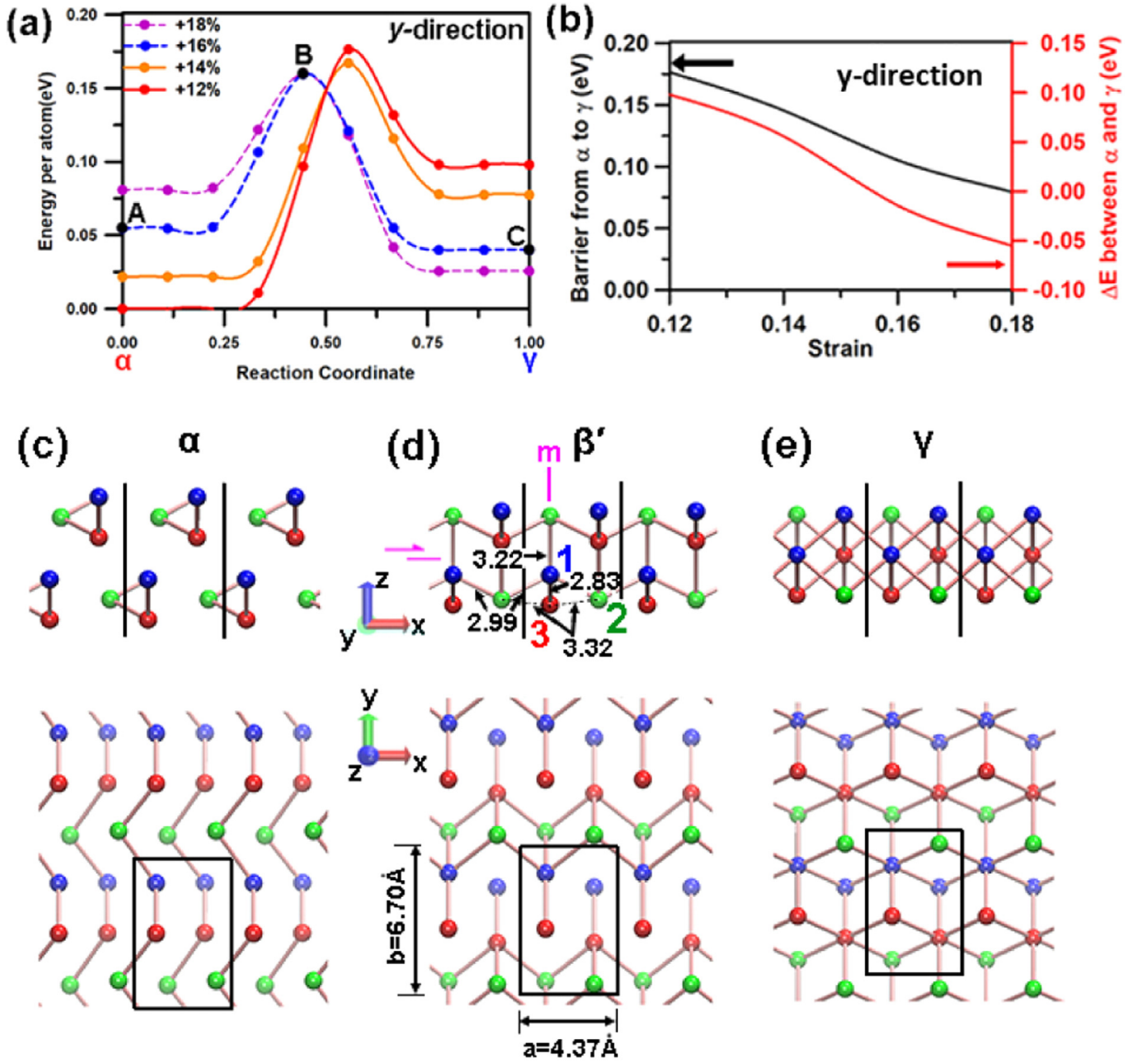

Fig. 8. The α→ γ phase transition: (a) shows the energy-reaction coordinate profiles for different strains along the chain direction; (b) shows the energy difference per atom between α- and γ-phase versus the tensile strain along the chain direction (red line). The energy barrier for the α→ γ phase transition versus the tensile strain (black line) is also illustrated in the figure. (c) - (e) show the atomic configurations of the α-, β′- and γ-phases, corresponding to point A, B and C in (a), respectively. The magenta half arrow in (d) shows the twofold screw axis along the *x*-direction and the magenta vertical line indicates a mirror plane (*m*). Atomic bond lengths are also shown in the unit of Å in (d).

(Fig. 7**e**), resulting in the change of the CLQB interaction in the α-phase to the covalent bonding in the β-phase. The corresponding changes in bond length and electron localization functions are also shown in Fig. 7**e** and **f**.

In Fig. 7**a** and **b**, the β-phase energy is always higher than that of the α-phase for all compressive and tensile strains. This energy difference is further enlarged by tensile strains but decreased by compressive strains. This phenomenon is also illustrated by the energy versus strain curves shown by the dashed lines in Fig. 7**c** and **d**. Additionally, the fractional distance *d* (defined in Fig. 2**a**) changes dramatically due to strain, as illustrated by the red line in Fig. 7**c** and **d**. For example, the value of *d* is about 0.39 under a strain of 9% along the *x*-direction, compared with 0.43 in the strain-free state. It is evident that under a compressive strain of over 6% in the *x*-direction or 9% in the *y*-direction, the energy of the α-phase is almost the same as that of the β-phase. Further compression (over 9% in the *x*-direction or 12% in the *y*-direction) causes the fractional distance *d* reaching 0.5 (see the intersection of black dotted lines and red solid lines in Fig. 7**c** and **d**), leading to a spontaneous α → β phase transition. On the contrary, under tensile strains, the α-phase always has lower energies than the β-phase. Specifically, the *x*-direction tensile strain leads to a rapid increase of the energy difference between the α- and β-phases (Fig. 7**c**), while the *y*-direction tensile strain almost maintains their energy difference (about 5–6 meV/atom, Fig. 7**d**). Overall, the energy difference between the two phases is comparable to or even much less than the thermal energy *kT*, depending on the in-plane strain direction applied. This suggests that the α → β phase transition can readily happen at room temperature under mechanical strains.

It has been reported that the 2-D Te film grown on the highly oriented pyrolytic graphite (HOPG) substrate presented the β-like phase with the lattice constants $a = 4.26$ Å and $b = 5.42$ Å [2], while other studies found $a = 4.45$ Å and $b = 5.93$ Å for the 2-D Te grown on graphene [22]. The 2-D Te film synthesized by the substrate-free solution method [1] tends to be an α-phase with the lattice constants $a = 4.3$ Å and $b = 6$ Å. In our DFT calculations, we find that $a = 4.33$ Å and $b = 5.78$ Å for the α-phase (Fig. 7**e**), and $a = 4.26$ Å and b

= 5.77 Å for the β-phase (Fig. 7**f**). If the effects of the finite temperature and lattice mismatch on different substrates are considered, we anticipate that the 2-D Te film in the first study [2] was under a compressive strain of at least 2% in the *x*-direction and 6.2% in the *y*-direction, while the lattice constants measured in the 2-D Te films in the latter two studies, i.e., either on the graphene substrate [22] or in the substrate-free case [1], are closer to our DFT calculations for the free-standing 2-D Te slabs. As a result, the seemingly compressed film in the first study is more β-like, while the latter two experimental cases are more α-like. In the first study, the authors also mentioned that larger lattice constants (and more α-like phase) were observed using thicker Te films. They attribute this phenomenon to a thickness-dependent phase transition from β to α [2]. Here we propose an alternative explanation: the HOPG substrate applies a compression strain to the thin Te film, leading to more β-like phase. However, the range of the interaction between the substrate and the film is limited. Thus the free end surface of Te thick slab becomes more and more α-like.

Another interesting feature of α → β phase transition is that this transition is from a chiral structure (α-phase) to a non-chiral one (β-phase). It is known that the right-handed α helical chain (Fig. 7**e**) is non-superposable to its mirror image: the left-handed α helical chain (Fig. 7**g**), while the β-phase is centrosymmetric (Fig. 7**f**). Given the fact that the energy difference between the α- and β-phases are comparable to the ambient thermal energy k_BT, which is only about 25 meV, we suggest that the transition between the left-handed and right-handed chiral structures in the α-phase could easily proceed through the intermediate β-phase.

3.3.2. The α→ γ phase transition

As we discussed previously, the in-plane tensile strain always makes the α-phase more stable than the β-phase. However, when the tensile strain along the *y*-direction exceeds some critical value, ca. 12%, the α-phase will no longer be stable and a possible α → γ phase transition will happen. Tensile strains along the *x*-direction could not lead to the α → γ phase transition, thus we only focus on the variation of the tensile strain along the *y*-direction. Similar to the α→β phase transition study, we take the 2 *L* α-phase as a working example. Fig. 8**a** shows the energy-reaction coordinate curves between the α- and γ-phases under different large tensile strains. Energy peaks are located close to the middle of the reaction coordinate, corresponding to an intermediate transition state. The atomic configurations of the α-phase, the γ-phase, and the transition state under a tensile strain of 16% along the *y*-direction are illustrated in the Fig. 8**c**, 8**e,** and **d**, respectively. As the transition state has the same space group ($P2_1/m$) and symmetry elements to the β-phase, i.e., the twofold screw axis along the *x*-direction and a mirror plane perpendicular to it (Fig. 8**d**), we name it as the β′-phase. However, this transition state has different lattice constants compared with those of the β-phase. Moreover, the mid-*layer* green atom "2" (see Fig. 8**d**) has a larger distance away from the lower-*layer* red atom "3" (about 3.32 Å) than the upper-*layer* blue atom "1" (about 2.99 Å, also see Fig. 8**d**), which is also distinct from the equal distance of about 3.06 Å in the β-phase (Fig. 3**a**). From Fig. 8**c** to Fig. 8**e,** it is seen that the α→ γ phase transition is essentially a 2 *L* α →1 *L* γ phase transition. Fig. 8**a** shows that the uniaxial tensile strain along the *y*-direction has a significant effect on the α→γ phase transition. A tensile strain under 15% makes the α-phase energy always lower than that of the γ-phase, while a tensile strain beyond 15% reverses this thermodynamic stability. This trend can also be directly observed from Fig. 8**b** (red line). Here we define the energy difference ΔE as ($E_\gamma - E_\alpha$)/atom, which exhibits a descending trend with the increase of the tensile strain. The energy barrier for the α→γ phase transition versus the tensile strain (the black curve in Fig. 8**b**) also shows a descending trend from 176.5 meV/atom to 79.5 meV/atom as the tensile strain is increased from 12% to 18%.

4. Discussion and conclusions

Our DFT calculations on the elemental 2-D tellurene reveal the following interesting features: (1) The 2-D tellurene could be formed in multiple phases, classified by their characteristic space groups and symmetry elements. The detailed atomic surface reconstruction, especially for the multiple *Layers* α- and δ-phases, has been illustrated. The relationships between these 2-D Te phases and the Te bulk have also been investigated; (2) The complex interatomic interactions in these distinct phases, such as the different types of covalent bonding and the CLQB interactions, result in dramatically different elastic modulus for each phase; (3) At present we have identified two possible phase transitions, i.e., the α → β and α → γ phase transitions; (4) Compression of the α-phase along any in-plane direction promotes the α → β phase transition, while in-plane tensile strains always make the α-phase more stable than the β-phase. However, the energy difference between the two phases is comparable to or even much smaller than the thermal energy *kT*, depending on the in-plane strain direction; and (5) the large elongation along the chain direction in the α-phase facilitates the α → γ phase transition. A transition state β′-phase has been identified, whose property needs to be further investigated. Our findings explain why different experimental groups may obtain different 2-D Te phases, revealing the substrate chosen may have a significant impact on the 2-D Te phases. Elastic modulus for each phase and the switch between different stable states due to strain modulation has also been investigated. This work is expected to shed light on the application of 2-D Te as high-performance functional materials in electronics, optoelectronics, and piezotronics.

There are many other interesting questions left for further studies. For example, two additional 2-D tellurene phases have also been reported in the literature, the 2H-MoS_2-like [10], and square-like [6] 2-D Te. Our initial DFT calculations show that these two phases have relatively high formation energy. However, their stability, properties, and possible phase transition mechanism may worth further investigations. Moreover, the effect of defects such as grain boundaries in 2-D Te materials should be explored in the future.

Acknowledgments

This work is partially supported by the National Science Foundation (NSF) (Grant No. 1609902) and the resources of the National Energy Research Scientific Computing Center, a DOE Office of Science User Facility supported by the Office of Science of the U.S. Department of Energy under Contract No. DE-AC02–05CH11231. W. Z. W. was partially supported by the National Science Foundation under grant CMMI-1762698.

Appendix A. Supplementary material

Supplementary data associated with this article can be found in the online version at doi:10.1016/j.nanoen.2019.01.040.

References

[1] Y.X. Wang, G. Qiu, R.X. Wang, S.Y. Huang, Q.X. Wang, Y.Y. Liu, Y.C. Du, W.A. Goddard, M.J. Kim, X.F. Xu, P.D. Ye, W.Z. Wu, Nat. Electron. 1 (4) (2018) 228–236.
[2] J.L. Chen, Y.W. Dai, Y.Q. Ma, X.Q. Dai, W.K. Ho, M.H. Xie, Nanoscale 9 (41) (2017) 15945–15948.
[3] Z.B. Gao, F. Tao, J. Ren, Nanoscale 10 (27) (2018) 12997–13003.
[4] X.H. Wang, D.W. Wang, A.J. Yang, N. Koratkar, J.F. Chu, P.L. Lv, M.Z. Rong, Phys. Chem. Chem. Phys. 20 (6) (2018) 4058–4066.
[5] B.Z. Wu, X.H. Liu, J.R. Yin, H. Lee, Mater. Res. Express 4 (9) (2017) 8.
[6] L.D. Xian, A.P. Paz, E. Bianco, P.M. Ajayan, A. Rubio, 2d Mater. 4 (4) (2017) 7.
[7] X.X. Xue, Y.X. Feng, L. Liao, Q.J. Chen, D. Wang, L.M. Tang, K.Q. Chen, J. Phys.-Condens. Matter 30 (12) (2018) 11.
[8] J.H. Yan, X.Y. Zhang, Y.Y. Pan, J.Z. Li, B.W. Shi, S.Q. Liu, J. Yang, Z.G. Song, H. Zhang, M. Ye, R.G. Quhe, Y.Y. Wang, J.B. Yang, F. Pan, J. Lu, J. Mater. Chem. C 6 (23) (2018) 6153–6163.

[9] S.J. Yang, B. Chen, Y. Qin, Y. Zhou, L. Liu, M. Durso, H.L. Zhuang, Y.X. Shen, S. Tongay, Phys. Rev. Mater. 2 (10) (2018) 8.
[10] Z.L. Zhu, X.L. Cai, S.H. Yi, J.L. Chen, Y.W. Dai, C.Y. Niu, Z.X. Guo, M.H. Xie, F. Liu, J.H. Cho, Y. Jia, Z.Y. Zhang, Phys. Rev. Lett. 119 (10) (2017) 5.
[11] C.S. Lin, W.D. Cheng, G.L. Chai, H. Zhang, Phys. Chem. Chem. Phys. 20 (37) (2018) 24250–24256.
[12] G. Qiu, Y.X. Wang, Y.F. Nie, Y.P. Zheng, K. Cho, W.Z. Wu, P.D.D. Ye, Nano Lett. 18 (9) (2018) 5760–5767.
[13] W.Z. Wu, G. Qiu, Y.X. Wang, R.X. Wang, P.D. Ye, Chem. Soc. Rev. 47 (19) (2018) 7203–7212.
[14] Y.Y. Pan, S.Y. Gao, L. Yang, J. Lu, Phys. Rev. B 98 (8) (2018) 9.
[15] Y. Wang, C.C. Xiao, M.G. Chen, C.Q. Hu, J.D. Zou, C. Wu, J.Z. Jiang, S.Y.A. Yang, Y.H. Lu, W. Ji, Mater. Horiz. 5 (3) (2018) 521–528.
[16] S.H. Yi, Z.L. Zhu, X.L. Cai, Y. Jia, J.H. Cho, Inorg. Chem. 57 (9) (2018) 5083–5088.
[17] Y.C. Du, G. Qiu, Y.X. Wang, M.W. Si, X.F. Xu, W.Z. Wu, P.D.D. Ye, Nano Lett. 17 (6) (2017) 3965–3973.
[18] S.J. Gao, Y.X. Wang, R.X. Wang, W.Z. Wu, Semicond. Sci. Technol. 32 (10) (2017) 9.
[19] Y. Wang, R. de Souza Borges Ferreira, R. Wang, G. Qiu, G. Li, Y. Qin, P.D. Ye, A. Sabbaghi, W. Wu, Nano Energy 57 (2019) 480–491.
[20] J.S. Qiao, Y.H. Pan, F. Yang, C. Wang, Y. Chai, W. Ji, Sci. Bull. 63 (3) (2018) 159–168.
[21] A. Coker, T. Lee, T.P. Das, Phys. Rev. B 22 (6) (1980) 2968–2975.
[22] X.C. Huang, J.Q. Guan, Z.J. Lin, B. Liu, S.Y. Xing, W.H. Wang, J.D. Guo, Nano Lett. 17 (8) (2017) 4619–4623.
[23] W.G. Dawson, D.W. Bullett, J. Phys. C -Solid State Phys. 20 (36) (1987) 6159–6174.
[24] J. Heising, M.G. Kanatzidis, J. Am. Chem. Soc. 121 (4) (1999) 638–643.
[25] H.H. Huang, X.F. Fan, D.J. Singh, H. Chen, Q. Jiang, W.T. Zheng, Phys. Chem. Chem. Phys. 18 (5) (2016) 4086–4094.
[26] B. Amin, T.P. Kaloni, U. Schwingenschlogl, RSC Adv. 4 (65) (2014) 34561–34565.
[27] F. Guller, A.M. Llois, J. Goniakowski, C. Noguera, Phys. Rev. B 91 (7) (2015) 7.
[28] Y.F. Chen, J.Y. Xi, D.O. Dumcenco, Z. Liu, K. Suenaga, D. Wang, Z.G. Shuai, Y.S. Huang, L.M. Xie, ACS Nano 7 (5) (2013) 4610–4616.
[29] L. Debbichi, O. Eriksson, S. Lebegue, Phys. Rev. B 89 (20) (2014) 5.
[30] N. Lu, H.Y. Guo, L. Li, J. Dai, L. Wang, W.N. Mei, X.J. Wu, X.C. Zeng, Nanoscale 6 (5) (2014) 2879–2886.
[31] J. Feng, X.F. Qian, C.W. Huang, J. Li, Nat. Photonics 6 (12) (2012) 865–871.
[32] X.F. Fan, C.H. Chang, W.T. Zheng, J.L. Kuo, D.J. Singh, J. Phys. Chem. C 119 (19) (2015) 10189–10196.
[33] A.B. Kaul, J. Mater. Res. 29 (3) (2014) 348–361.
[34] K.A.N. Duerloo, Y. Li, E.J. Reed, Nat. Commun. 5 (2014) 9.
[35] A. Ambrosi, Z. Sofer, M. Pumera, Chem. Commun. 51 (40) (2015) 8450–8453.
[36] H. Wang, L.L. Yu, Y.H. Lee, Y.M. Shi, A. Hsu, M.L. Chin, L.J. Li, M. Dubey, J. Kong, T. Palacios, Nano Lett. 12 (9) (2012) 4674–4680.
[37] Y.C. Lin, D.O. Dumcencon, Y.S. Huang, K. Suenaga, Nat. Nanotechnol. 9 (5) (2014) 391–396.
[38] W.Z. Wu, Z.L. Wang, Nat. Rev. Mater. 1 (7) (2016) 17.
[39] G. Kresse, J. Furthmuller, Phys. Rev. B 54 (16) (1996) 11169–11186.
[40] P.E. Blochl, Phys. Rev. B 50 (24) (1994) 17953–17979.
[41] G. Kresse, D. Joubert, Phys. Rev. B 59 (3) (1999) 1758–1775.
[42] J.P. Perdew, K. Burke, M. Ernzerhof, Phys. Rev. Lett. 77 (18) (1996) 3865–3868.
[43] J.P. Perdew, J.A. Chevary, S.H. Vosko, K.A. Jackson, M.R. Pederson, D.J. Singh, C. Fiolhais, Phys. Rev. B 46 (11) (1992) 6671–6687.
[44] A. Tkatchenko, M. Scheffler, Phys. Rev. Lett. 102 (7) (2009) 4.
[45] S. Grimme, J. Comput. Chem. 27 (15) (2006) 1787–1799.
[46] S. Grimme, S. Ehrlich, L. Goerigk, J. Comput. Chem. 32 (7) (2011) 1456–1465.
[47] H.J. Monkhorst, J.D. Pack, Phys. Rev. B 13 (12) (1976) 5188–5192.
[48] G. Henkelman, B.P. Uberuaga, H. Jonsson, J. Chem. Phys. 113 (22) (2000) 9901–9904.
[49] J.S. Qiao, X.H. Kong, Z.X. Hu, F. Yang, W. Ji, Nat. Commun. 5 (2014) 7.
[50] Z.X. Hu, X.H. Kong, J.S. Qiao, B. Normand, W. Ji, Nanoscale 8 (5) (2016) 2740–2750.
[51] F.M. Norman, L. Kathleen, International Tables for X-Ray Crystallography 1 The Kynoch Press, Birmingham, UK, 1952.
[52] T. Hahn, International Tables for Crystallography Vol. A Springer-Verlag, New York, NY, 1983.
[53] S. Bertolazzi, J. Brivio, A. Kis, ACS Nano 5 (12) (2011) 9703–9709.
[54] C. Lee, X.D. Wei, J.W. Kysar, J. Hone, Science 321 (5887) (2008) 385–388.
[55] H.L.L. Zhuang, R.G. Hennig, Chem. Mater. 25 (15) (2013) 3232–3238.
[56] H. Sahin, S. Cahangirov, M. Topsakal, E. Bekaroglu, E. Akturk, R.T. Senger, S. Ciraci, Phys. Rev. B 80 (15) (2009) 12.
[57] J.W. Jiang, H.S. Park, J. Phys. D.-Appl. Phys. 47 (38) (2014) 3.
[58] J. Tao, W.F. Shen, S. Wu, L. Liu, Z.H. Feng, C. Wang, C.G. Hu, P. Yao, H. Zhang, W. Pang, X.X. Duan, J. Liu, C.W. Zhou, D.H. Zhang, ACS Nano 9 (11) (2015) 11362–11370.

Dr. Yuan Xiang is a research associate in Yongsheng Leng's research group at The George Washington University. He received a Diplôme d'ingénieur at Ecole Centrale de Lyon, France and an M.S. in Mechanics Theory and Design at Southwest Jiaotong University, China. He obtained his Ph.D. degree at The George Washington University in 2016. His research interests include computational simulation and theory for membrane science, metal/semiconductor contacts, molecular electronics, nanotribology, and functional nanomaterials for energy harvesting.

Shengjie Gao received his BS degree in Materials Chemistry from Lanzhou University, China in 2016. He is currently working towards his PhD degree at School of Industrial Engineering in Purdue University under the supervision of Dr. Wenzhuo Wu. His current research interests mainly focus on the characterization of low-dimensional piezoelectric/ferroelectric materials, design of self-powered smart system and its application in Human-Computer Interface.

Dr. Rong-Guang Xu is currently a research associate in Professor Yongsheng Leng's research group. He also earned his Ph.D. degree in the same group at The George Washington University. He received his B.S. degree in Applied Physics from Wuhan University, China. His research expertise includes multi-scale computational physics, materials science and mechanics. His research interests include computational simulation and modeling of mechanical properties of liquid films in confined geometry, nanotribology, micromechanics of interfaces, and 2D materials.

Yongsheng Leng earned his Ph.D. from Tsinghua University. He now is a professor at The George Washington University, Washington, DC. Through theory and computer simulations, his research has been evolving from contact mechanics and tribology to more fundamental questions in surface and interfacial science, including liquid structure and dynamics under nanometers confinements, computational nanotribology, membrane fouling mechanisms in water purification, clay swelling in oil and gas recovery, and the structure, dynamics, and transport properties of single molecular junctions in molecular electronics devices and metal/semiconductor contacts in energy harvesting system.

Dr Wenzhuo Wu is the Ravi and Eleanor Talwar Rising Star Assistant Professor in School of Industrial Engineering at Purdue University. He received his BS in Electronic Information Science and Technology in 2005 from the University of Science and Technology of China (USTC), Hefei and his ME in Electrical and Computer Engineering from the National University of Singapore (NUS) in 2008. Dr Wu received his Ph.D. from Georgia Institute of Technology in Materials Science and Engineering in 2013. Dr Wu's research interests include design, manufacturing, and integration of 1D and 2D nanomaterials for applications in energy, electronics, optoelectronics, and wearable devices. He was a recipient of the Oak Ridge Associated Universities (ORAU) Ralph E. Powe Junior Faculty Enhancement Award in 2016, and the IOP Semiconductor Science and Technology Best Early Career Research in 2017.